

# Insights from a zeroth order analysis on steady streaming generated by an oscillating gas slug

Shambhu Anil\* and Pushpavanam Subramaniam<sup>†</sup>

*Department of Chemical Engineering,  
Indian Institute of Technology, Madras, Chennai, 600036, India.*

(Dated: September 21, 2021)

## Abstract

Active micropumping and micromixing using oscillating bubbles form the basis for various Lab – on – chip applications. Acoustically oscillating bubbles are commonly used in active particle sorting and in micropumps/mixers. Slug flow is a commonly observed flow – regime in gas – liquid flows. In this work, we theoretically find the streaming intensity produced in a confined continuous liquid phase by an acoustically oscillating stationary gas slug undergoing surface mode oscillations. We explicitly specify the interface oscillation and compute the surface mode amplitudes by solving the momentum and continuity equations. The resonant frequency is found to be consistent with that reported experimentally in the literature. The variation of streaming intensity with tube diameter is found to be identical to that reported by K. Ryu, S. K. Chung, S. K. Cho; Journal of the Association for Laboratory Automation, Vol. 15 (3), 163 (2010). Although the leading order solution is purely oscillatory in nature, the streaming intensity estimated is found to be proportional to actual streaming velocity. The effect of slug size on resonant frequency of system is also studied.

## I. INTRODUCTION

Steady streaming is the observable flow induced in a fluid when it is excited by an oscillatory input [1]. This is induced by the non-oscillatory nature of Reynolds stress and has been extensively investigated in the context of studying the effect of ultrasound in microfluidic devices [2]. Acoustic energy can directly or indirectly interact with fluids and generate motion. Eckart streaming is that caused by the direct dissipation of acoustic energy into the bulk of the fluid. This is a macroscale phenomenon and is of less significance in microfluidic experiments as it requires the length scale of the system to be very high compared to the wavelength of the driving source. Schlichting streaming is the flow induced in wall boundary layers by viscous dissipation of acoustic energy. The associated flow in bulk driven by this boundary layer flow is Rayleigh streaming. Both these flows are characterized by counter – rotating vortices in the bulk and wall boundary layer. Rayleigh and Schlichting streaming have been extensively used in various lab – on – chip devices for applications in cell trapping

---

\* shambhu.anilkumar@gmail.com

† spush@iitm.ac.in

using surface acoustic waves [3], particle or cell trapping in PDMS (Polydimethylsiloxane) channels using soft wall protrusions [4] and micro-mixing [5]. These applications require high frequency of sound and fabrication of intricate experimental setups.

To overcome these limitations, several researchers have explored an alternate way of doing active lab-on-chip operations based on acoustically excited microbubbles [6]. The experimental setup typically consists of a deformable microchannel (PDMS and Ecoflex [7]) attached to a glass substrate on which a piezoelectric transducer is embedded. The gas bubble is either suspended in the liquid or anchored on the microchannel depending on the application involved. On activating the piezo transducer, the bubble oscillates or translates with interface deformation. The steady streaming caused by such oscillating microbubbles is called cavitation microstreaming [8]. It is characterized by the formation of several closed vortices around the bubble and has applications in Lab – on – Chip devices from particle manipulation and sorting [9] to microparticle rotation [10] and drug delivery [11]. The phenomenon of cavitation microstreaming has been extensively studied using analytical and semi analytical techniques for various applications.

Davidson & Riley [8] obtained an analytical solution to flow produced by a laterally oscillating rigid bubble. Longuet Higgins [12] extended this study by considering a rigid bubble undergoing both lateral and radial oscillations. It was observed that the streaming velocity peaked when both lateral and radial oscillations were out of phase. Elder [13] experimentally found the relevant parameters that affect cavitation microstreaming and analyzed the effect of each parameter in the flow velocity induced. Elder concluded that a significant contribution to streaming arose from volumetric oscillations of the bubble. Tho *et.al.* [14] studied and quantified the flow field induced by single and multiple bubbles. This study confirmed that the modes formed on the surface of the bubble (surface mode oscillations) determined the number of closed vortices formed around the bubble and magnitude of streaming velocity. It was also found that with increase in frequency, the bubble underwent linear, elliptical then circular translation. This caused vortical followed by simple azimuthal flow around the bubble.

Wang *et.al.* [4] found the mode amplitudes on the surface of a sessile semi – cylindrical

microbubble experimentally and compared it with a semi – analytical solution using perturbation and matched asymptotic techniques. Here a bubble is lodged in a side channel of a microfluidic system forcing the fluid to circulate or get pushed away from the bubble. This channel geometry has various applications in micromixing [5], micropumping [15] and particle sorting and trapping [9], [16]. It was also found by Wang *et.al.* [4] that the surface modes on the bubble increase with frequency.

Rallabandi *et.al.* [17] studied the microstreaming generated by surface oscillations of a sessile semi – cylindrical microbubble and established a theoretical framework for the experimental setup investigated by Wang *et al.* This semi - analytical study proved that the interaction of different surface modes is responsible for the fountain like fluid ejection from the bubble. At higher frequencies however, the pattern reversed because of wall effects.

Gas slugs are used in mass transfer limited reactions, drug delivery and other pharmaceutical operations in Lab- on-chip devices [18]. Previous studies focusing on combining gas slugs with acoustic streaming, have analysed applications in particles separation [9] and micromixing [19]. Mohanty *et.al.* [20] developed micropropellers powered by oscillating microbubbles. The targeted movement of these propellers is achieved by angling the propelling bubbles. Yang *et.al.* [21] found that the interface oscillation and periodic slug length fluctuation in a slug flow microreactor subjected to acoustic field can intensively affect the recirculation in the liquid slug. This in turn enhances the mass transfer coefficient of such slug flow micro reactors. A semi – empirical formula was also developed to represent the new mass transfer coefficient in terms of acoustic power, density and Reynolds number.

Ryu *et.al.* [15] experimentally measured the flow rate and velocity produced in a tube kept vertically above an oscillating sessile bubble. Fauconnier *et.al.* [22] categorically studied the interface deformation due to bubble oscillation of such a wall attached microbubble. It was found that modal interaction between zonal, tesseral and sectoral modes is key to quantifying the interfacial deformation. This is similar to the concept of mixed mode streaming proposed by Rallabandi *et.al.* [17] However, there is a dearth of analytical studies on the commonly used channel geometries for micropumping and micromixing. This motivates us to analyse the streaming induced by a trapped slug in a microchannel. Our objective here

is to introduce a minimalistic model that predicts the resonant frequency and velocity field produced by the slug.

In this study, we focus on a gas slug trapped along a microchannel. It induces closed vortices on the continuous phase fluid once the transducer is activated. We estimate the flow field intensity by determining the order of magnitude of the Reynolds stress. For this, we find the maximum magnitude of Reynolds stress produced by the interaction of each surface mode with the volumetric mode [4]. We also compare the qualitative trends of our results with the experiments of Ryu *et.al.* [15] and find a correlation between measured velocity with the calculated intensity. The formulation used in this study is similar to that used by Wang *et.al.* [4] However, we determine the effect of slug length and width on the resonant frequency of the system. We show the similarity in variation of Minnaert frequency of a prolate spheroid with that of a trapped rectangular slug analysed in our work.

We discuss the formulation of the theoretical model used in Section 2 of this paper. Section 3 describes the characteristic scales and governing equations used for solving this model. Section 4 details the solution to the leading order velocity field for high Strouhal numbers using perturbation techniques and matched asymptotic expansions. Section 5 discusses the results and major findings of this study and Section 6 summarises this work and its major contributions.

## II. PROBLEM FORMULATION

In this work, we determine the flow field intensity generated by a trapped slow – oscillating bubble. The geometry considered mimics an acoustic micropump. For this, we model the bubble to be a rectangular – shaped slug, as shown in the schematic (Figure 1). We assume the interface to be flat at steady state i.e., the contact angle to be 90 degrees. This can be experimentally realized by including angled groves (necks) along the walls of the microchannel to control the contact angle and using plasma treatment for etching [23].

We restrict the analysis to two – dimensions assuming the extent to be infinite in  $z$  direction as shown in the Figure 1. The deformation of the interface is explicitly given as a

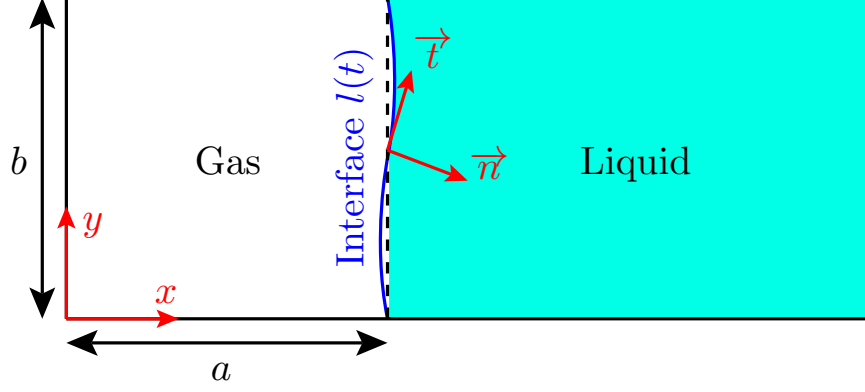


FIG. 1: A schematic of the system under consideration

periodically oscillating function  $l(t)$ .

$$l(t) = a(1 - \epsilon i h(y) e^{i\omega t}) \quad (1)$$

Here  $a$  is the length of the bubble/slug when it is undisturbed (See Figure 1).  $\epsilon$  is the ratio of amplitude of oscillation to the base slug length.  $h(y)$  specifies the deformation of the interface, and  $\omega$  denotes the angular frequency of oscillation of the bubble. We assume that the amplitude of deformation is much lower than the length of the slug. Thus,  $\epsilon \ll 1$  and this enables us to carry out an analysis of the system based on perturbation methods and asymptotics. We also assume that the gas is compressible, and its expansion and contraction is governed by polytropic law. We also assume the liquid to be incompressible and the interface to be pinned to the walls of the microchannel ( $h(0) = h(1) = 0$ ). These assumptions allow us to analyse the system in rectangular cartesian coordinates, while retaining the important physics involved.

### III. GOVERNING EQUATIONS AND CHARACTERISTIC SCALES

The flow field in the liquid is obtained from the continuity equation (2) and the Navier Stokes equation (3, 4)

$$\nabla \cdot \mathbf{u} = 0 \quad (2)$$

$$\rho \left( \frac{\partial u}{\partial t} + \mathbf{u} \cdot \nabla u \right) = -\frac{\partial p}{\partial x} + \mu \left( \frac{\partial^2}{\partial x^2} + \frac{\partial^2}{\partial y^2} \right) u \quad (3)$$

$$\rho \left( \frac{\partial v}{\partial t} + \mathbf{u} \cdot \nabla v \right) = -\frac{\partial p}{\partial y} + \mu \left( \frac{\partial^2}{\partial x^2} + \frac{\partial^2}{\partial y^2} \right) v \quad (4)$$

This system of equations is subject to the following boundary conditions:

1. At walls:

(a) No slip and no penetration at walls:  $u = v = 0$  at  $y = 0, b$ , where  $b$  is the width between the channels

2. At liquid - gas interface:

(a) Zero tangential Stress at interface:  $\mathbf{n} \cdot \mathbf{T} \cdot \mathbf{t} = 0$  at  $x = l(t, y)$

(b) Kinematic condition at the interface:  $\frac{\partial F}{\partial t} \frac{1}{|\nabla F|} + \mathbf{u} \cdot \mathbf{n} = 0$  at  $x = l(t, y)$ , where  $F = x - l(t, y)$  represents the interface deformation and  $\mathbf{n} = \frac{\nabla F}{|\nabla F|}$ .

(c) Normal stress balance at the interface:  $p_i - p + \tau_{xx} - \gamma\kappa|_{x=l(t,y)} = 0$

Here  $p$ ,  $u$ ,  $v$  are the pressure and velocity components along  $x$  and  $y$  directions respectively.  $\mathbf{n}$  and  $\mathbf{t}$  represent the normal and tangent vectors to the interface as shown in schematic (Figure 1).  $\mu$ ,  $\rho$  and  $\gamma$  are the viscosity, density and surface tension of the fluid used in the system.  $p_i$  and  $p$  are the pressure inside and outside the bubble.  $\tau_{xx}$  and  $\kappa$  are the normal viscous stress and curvature of the interface.  $\mathbf{T}$  represents the stress tensor at the interface.

To comprehensively understand the behavior of the system, we render the equations dimensionless. For this, the chosen length scales are,  $x_{ch} = a$  and  $y_{ch} = b$ . We choose the time scale,  $t_{ch} = \frac{1}{\omega}$  and the characteristic horizontal streaming velocity as  $\epsilon\omega a$ . Cavitation microstreaming occurs at large Strouhal numbers defined as  $St = \frac{\omega a}{U_s}$ . Here  $\omega a$  is the imposed velocity and,  $U_s$  is the streaming velocity observed. From definition of Strouhal number, we can also write  $\epsilon = St^{-1}$ . This is also an indicator of the order of magnitude of  $\epsilon$ . Subsequently, from continuity equation we get the vertical characteristic velocity as,  $v_{ch} = \epsilon\omega b$ . Non dimensionalizing the governing equations with this choice of characteristic scales, we get:

$$\frac{\partial u}{\partial t} + \epsilon \mathbf{u} \cdot \nabla u = -\frac{p_{ch}}{\epsilon \rho \omega^2 a^2} \frac{\partial p}{\partial x} + \frac{1}{Re} \left( \frac{\partial^2}{\partial x^2} + k^2 \frac{\partial^2}{\partial y^2} \right) u \quad (5)$$

$$\frac{\partial v}{\partial t} + \epsilon \mathbf{u} \cdot \nabla v = -\frac{p_{ch}}{\epsilon \rho \omega^2 b^2} \frac{\partial p}{\partial y} + \frac{1}{Re} \left( \frac{\partial^2}{\partial x^2} + k^2 \frac{\partial^2}{\partial y^2} \right) v \quad (6)$$

Here  $Re$  is the Reynolds number defined as  $\frac{\omega a^2}{\nu}$ .  $p_{ch}$  denotes a characteristic pressure.  $k$  is the aspect ratio of the bubble defined as:  $k = \frac{a}{b}$ . It is to be noted here that the characteristic pressure scale cannot be concluded from the present Navier Stokes equation. We will derive the exact pressure scale after calculating velocity using stream function formulation.

#### IV. METHOD OF SOLUTION

Our objective here is to obtain the streaming intensity of leading order flow field in the liquid. To do so, we need to solve the above system of non – dimensionalised equations and obtain the surface mode amplitudes using the normal stress balance. We use perturbation techniques and matched asymptotic expansions to find a composite solution throughout the domain. We divide the domain into two regions: *i*) an Inner region or Wall boundary layer and *ii*) Outer region or Bulk as shown in Figure 2. The leading order velocity field is found separately in each region and matched to obtain a composite solution throughout the domain. There is also a boundary layer close to the bubble interface. However, the flow field in the bubble boundary layer automatically appears in the bulk solution as a higher order term in  $\delta$  (Stokes's layer thickness defined as  $\delta = \frac{1}{a} \sqrt{\frac{\nu}{\omega}} = Re^{-\frac{1}{2}}$ ). Hence, the velocity field in the bubble boundary layer is not solved for explicitly. However, we assume that there is no overlap of wall and bubble boundary layer as the interface is pinned at the walls.

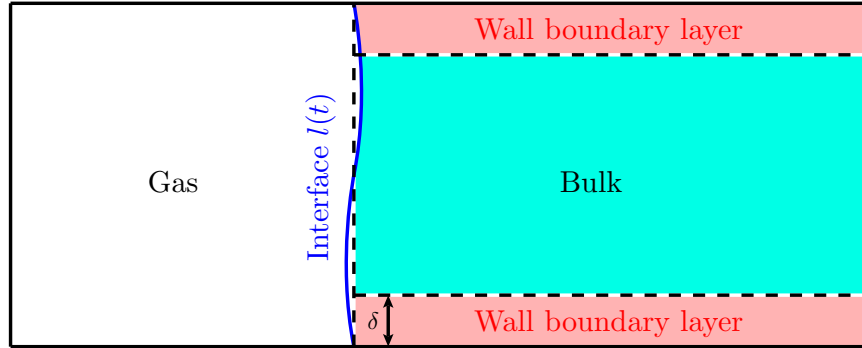


FIG. 2: The bulk and wall boundary layer region in the domain.

The governing system of equations is solved using perturbation techniques. Velocity and pressure are expanded in increasing order of  $\epsilon$  as:

$$\begin{aligned} u &= u_0 + \epsilon u_1 + O(\epsilon^2) \\ v &= v_0 + \epsilon v_1 + O(\epsilon^2) \\ p &= p_0 + \epsilon p_1 + O(\epsilon^2) \end{aligned} \tag{7}$$

In this work, the leading order problem is solved semi analytically with only  $\epsilon$  as the perturbation parameter.



### A. The leading order problem

We substitute the perturbation expansion (Equation 7) in governing equations 5, 6 and collect the terms of  $O(1)$  to obtain the leading order governing equations as:

$$\frac{\partial u_0}{\partial t} = -\frac{p_{ch}}{\epsilon\rho\omega^2 a^2} \frac{\partial p_0}{\partial x} + \frac{1}{Re} \left( \frac{\partial^2}{\partial x^2} + k^2 \frac{\partial^2}{\partial y^2} \right) u_0 \quad (8)$$

$$\frac{\partial v_0}{\partial t} = -\frac{p_{ch}}{\epsilon\rho\omega^2 b^2} \frac{\partial p_0}{\partial y} + \frac{1}{Re} \left( \frac{\partial^2}{\partial x^2} + k^2 \frac{\partial^2}{\partial y^2} \right) v_0 \quad (9)$$

The subscript 0 throughout the paper denotes the zeroth order variable. Exploiting the 2D nature of the flow field we seek solutions to the above equations using a stream function formulation. The leading order velocity in terms of stream function is given as:

$$u_0 = \frac{\partial \psi_0}{\partial y} \quad (10)$$

$$v_0 = -\frac{\partial \psi_0}{\partial x} \quad (11)$$

Here  $\psi_0$  is the leading order stream function. After eliminating pressure, a modified biharmonic equation in  $\psi_0$  is obtained as shown in Equation 12. The boundary conditions at the interface are defined for  $x = l(t)$ . We use domain perturbation around the steady flat interface to obtain the boundary conditions at  $x = 1$ .

$$\frac{\partial}{\partial t} \left( \frac{\partial^2}{\partial x^2} + k^2 \frac{\partial^2}{\partial y^2} \right) \psi_0 = \frac{1}{Re} \left( \frac{\partial^2}{\partial x^2} + k^2 \frac{\partial^2}{\partial y^2} \right)^2 \psi_0 \quad (12)$$

Alongside,

1. Kinematic boundary condition at interface:  $\frac{\partial \psi_0}{\partial y}|_{x=1} = h(y) e^{it}$
2. Tangential stress balance at interface:  $\frac{\partial^2 \psi_0}{\partial x^2} - k^2 \frac{\partial^2 \psi_0}{\partial y^2}|_{x=1} = 0$
3. No slip and no penetration at the walls:  $\frac{\partial \psi_0}{\partial y} = -\frac{\partial \psi_0}{\partial x} = 0$
4. Normal stress balance at the interface:  $p_i^{(0)} - p_0 + \tau_{xx}^{(0)} - \gamma\kappa|_{x=1} = 0$

### B. Outer solution

The outer solution or bulk solution is valid in a region where inertial effects are dominant. To solve this modified biharmonic equation, we seek solutions of the form:  $\psi_0 = f(x) e^{i\lambda y} e^{it}$ . The governing equation for  $f$  simplifies to

$$f''''(x) - (iRe + 2k^2\lambda^2) f''(x) + (k^4\lambda^4 + ik^2Re\lambda^2) f(x) = 0 \quad (13)$$

$f'$  denotes the derivative of  $f$  w.r.t.  $x$ . The general solution to this equation is given by:

$$f(x) = C_1 e^{\xi x} + C_2 e^{-\xi x} + C_3 e^{-k\lambda x} + C_4 e^{k\lambda x} \quad (14)$$

Here  $\xi = \sqrt{iRe + k^2\lambda^2}$ . The Reynolds number  $Re$  is related to Stokes's layer thickness  $\delta$  as  $Re = \frac{2}{\delta^2}$ . We can also define  $\xi = \sqrt{\alpha^2 + k^2\lambda^2}$  where  $\alpha = \frac{1+i}{\delta}$ . Since flow is bounded as  $x \rightarrow \infty$ , the constants  $C_1 = C_4 = 0$ .

$$f(x) = C_2 e^{-\xi x} + C_3 e^{-k\lambda x} \quad (15)$$

We obtain  $\lambda$  from no penetration boundary condition as  $\lambda = n\pi$ , such that  $n = 0, 1, 2, 3$ . Now,

$$\psi_0 = \sum_{n=0}^{\infty} (C_2 e^{-\xi x} + C_3 e^{-kn\pi x}) \sin n\pi y e^{it} \quad (16)$$

From kinematic and tangential boundary condition, we obtain the constants  $C_2$  and  $C_3$  as:

$$C_2 = \sum_{n=0}^{\infty} A_n i \delta^2 k^2 n \pi e^{\xi} \quad (17)$$

$$C_3 = \sum_{n=0}^{\infty} A_n \left( \frac{1}{n\pi} - i \delta^2 k^2 n \pi \right) e^{kn\pi} \quad (18)$$

The stream function solution for leading order in bulk takes the form:

$$\psi_0 = \sum_{n=0}^{\infty} A_n \left( \frac{1}{n\pi} e^{-kn\pi s} + i \delta^2 k^2 n \pi (e^{-\xi s} - e^{-kn\pi s}) \right) \sin n\pi y e^{it} \quad (19)$$

Here,  $s = x - 1$  and  $A_n$  is the amplitude of surface modes on the interface. The  $O(\delta^2)$  term in the expression represents the contribution from the bubble boundary layer. It is to be noted that although this is a small quantity, we retain it in the calculations forward because of the  $k^2$  term multiplying it.

While solving for this region, we do not impose the no slip boundary condition at the walls. Instead, we calculate the horizontal slip velocity at  $y = 0, 1$  in the bulk and match it with the boundary layer solution to obtain the composite velocity field throughout the domain.

### C. Inner solution

To solve in the wall boundary layer, the  $y$  variable is scaled as  $\eta = \frac{y}{\delta}$  and  $\eta = \frac{1-y}{\delta}$  for the bottom ( $y = 0$ ) and top ( $y = 1$ ) walls, respectively. The stream function  $\psi_0$  is also scaled as

$\psi_{bl} = \frac{\psi_0}{\delta}$ . This allows the flow in a small region close to the walls to be analyzed. This inner domain spans from  $\eta = 0$  at the walls to  $\eta = \infty$  as  $\delta \ll 1$ . The rescaled stream function formulation is given by:

$$\frac{\partial}{\partial t} \left( \frac{\partial^2}{\partial x^2} + \frac{k^2}{\delta^2} \frac{\partial^2}{\partial \eta^2} \right) \psi_{bl} = \frac{1}{Re} \left( \frac{\partial^2}{\partial x^2} + \frac{k^2}{\delta^2} \frac{\partial^2}{\partial \eta^2} \right)^2 \psi_{bl} \quad (20)$$

We seek  $\psi_{bl}$  as  $\psi_{bl} = g(x, \eta) e^{it}$  and impose no slip and no penetration boundary condition at the walls. The system of equations governing the flow in the wall boundary layer reduces to

$$\frac{2i}{k^2} \frac{\partial^2 g}{\partial \eta^2} = \frac{\partial^4 g}{\partial \eta^4} + O(\delta^2) \quad (21)$$

This is subject to:

1. No penetration boundary condition:  $\psi_{bl} = 0$  at  $\eta = 0$ .
2. Far field condition:  $\psi_{bl}$  is bounded at  $\eta = \infty$ .
3. No slip boundary condition:  $\frac{\partial \psi_{bl}}{\partial \eta} = 0$  at  $\eta = 0$ .

This yields a boundary layer flow field expression similar to the flow field obtained by Riley [1]. Riley analyzed the steady velocity induced close to a wall in the presence of far field oscillatory flow. Our solution matches that of Riley when aspect ratio,  $k = 1$ .

$$\psi_{bl} = C(x) \left( \eta - \frac{1-i}{2} \left( 1 - e^{\frac{-(1+i)\eta}{k}} \right) \right) e^{it} \quad (22)$$

We obtain the function  $C(x)$  by matching the horizontal velocity from bulk with boundary layer. It is to be noted that the vertical velocity obtained from the wall boundary layer solution is linearly increasing. However, it is considered negligible as it is of  $O(\delta)$ . So we match the dominant horizontal velocity as shown:

$$\frac{\partial \psi_{bl}}{\partial \eta} \Big|_{\eta \rightarrow \infty} = \frac{\partial \psi_0}{\partial y} \Big|_{y=0} \quad (23)$$

This gives us the final expression for wall boundary layer stream function as:

$$\psi_{bl} = \sum_{n=0}^{\infty} A_n \left( e^{-kn\pi s} + i\delta^2 k^2 n^2 \pi^2 (e^{-\xi s} - e^{-kn\pi s}) \right) \left( \eta - \frac{1-i}{2} \left( 1 - e^{\frac{-(1+i)\eta}{k}} \right) \right) e^{it} \quad (24)$$

Here  $\eta = y/\delta$  for the bottom wall and  $\eta = (1-y)/\delta$  for the top wall. Also  $s = x - 1$  and  $k$  is the aspect ratio of the slug.

#### D. Composite leading order solution

Having obtained the velocity in each of the region, we now determine the composite velocity field in the entire domain. The composite horizontal velocity field is obtained by matching the bulk and boundary layer expressions. The objective is to get a ‘union’ of velocity field between bulk and boundary layers. Since the velocity is continuous and purely horizontal at the edge of boundary layers  $y = \delta$  and  $y = 1 - \delta$  (See Figure 2), we can add the bulk and boundary layers’ velocity field and subtract the overlapping velocity to avoid double counting. This type of matching is called Prandtl matching.

$$u_{comp} = u_{bulk} + u_{bl} - (u_{bulk}|_{y=0} + u_{bulk}|_{y=1})$$

$$u_{comp} = \sum_{n=0}^{\infty} A_n \left( e^{-kn\pi s} + i\delta^2 k^2 n^2 \pi^2 (e^{-\xi s} - e^{-kn\pi s}) \right) \left( \cos n\pi y - e^{\frac{-(1+i)y}{k\delta}} - e^{\frac{-(1+i)(1-y)}{k\delta}} \right) e^{it} \quad (25)$$

Using this horizontal composite velocity (25) on the leading order kinematic boundary condition helps in determining the total deformation  $h(y)$  of the interface.

$$h(y) = \sum_{n=0}^{\infty} A_n \left( \cos n\pi y - e^{\frac{-(1+i)y}{k\delta}} - e^{\frac{-(1+i)(1-y)}{k\delta}} \right) e^{it} \quad (26)$$

The assumption of the pinned interface implies no boundary layer overlap. This condition essentially means  $h(y)$  must be zero at  $y = 0, 1$ . Consequently, the eigen values must only be even multiples of  $\pi$ . We address this by transforming  $n \rightarrow 2n$  in all equations. Using this, the final expression for velocity field and interface deformation in the leading order is given as:

$$\mathbf{u}_0 = \sum_{n=0}^{\infty} A_n \left( e^{-2kn\pi s} + 4i\delta^2 k^2 n^2 \pi^2 (e^{-\xi_n s} - e^{-2kn\pi s}) \right) e^{it} \left( \left( \cos 2n\pi y - e^{\frac{-(1+i)y}{k\delta}} - e^{\frac{-(1+i)(1-y)}{k\delta}} \right) \mathbf{i} + \sin 2n\pi y \mathbf{j} \right) \quad (27)$$

$$h(y) = \sum_{n=0}^{\infty} A_n \left( \cos 2n\pi y - e^{\frac{-(1+i)y}{k\delta}} - e^{\frac{-(1+i)(1-y)}{k\delta}} \right) e^{it} \quad (28)$$

Here  $\xi_n = \sqrt{iRe + 4k^2 n^2 \pi^2}$ . Having obtained the overall deformation of the interface, the amplitudes  $A_n$  are obtained using normal stress balance boundary condition at the interface.

### E. Finding surface mode amplitudes of interface deformation

Our next objective is to find the amplitudes of each mode of interface oscillation ( $A_n$ ) as shown in Equation 27 , 28. To do so, we employ normal stress balance condition at the interface given by:

$$p_i^{(0)} - p_0 + \tau_{xx}^{(0)} - \gamma\kappa|_{s=0} = 0 \quad (29)$$

It is to be noted that the actual boundary condition is to be imposed at  $x = l(t)$ . However, after domain perturbation, we obtain Equation 29 with the leading order velocity and pressure field. This requires us to compute the pressure inside and outside the bubble, curvature of interface and the viscous stress at the interface. The fluid pressure just outside the interface ( $p_0|_{s=0}$ ) is found by substituting the composite velocity field into the leading order governing equation and solving for pressure.

$$p_o|_{s=0} = \rho\epsilon\omega^2 a^2 \left( \sum_{n=1}^{\infty} A_n i \left( \frac{4kn\pi}{\alpha^2} + \frac{1}{2kn\pi} \right) \cos 2n\pi y + p_0^* \right) e^{it} \quad (30)$$

We determine the pressure inside the bubble assuming that it undergoes polytropic expansion and contraction. ( $PV_{initial}^\eta = PV_{final}^\eta$ ). This gives us the relative pressure inside the bubble as

$$p_i^0 = p_0 i\epsilon\eta e^{it} \left( A_0 + \sum_{n=0}^{\infty} \frac{2A_n k}{\alpha} \left( e^{-\frac{\alpha}{k}} - 1 \right) \right) \quad (31)$$

The dimensional viscous stress tensor component ( $\tau_{xx}$ ) is determined as:

$$\tau_{xx} = \epsilon\omega \left( \mu \frac{\partial u_{comp}}{\partial x} \right) = \mu\epsilon\omega \sum_{n=0}^{\infty} A_n \left( -2kn\pi e^{-2kn\pi s} + 4in^2\pi^2\delta^2 k^2 \left( -\xi_n e^{-\xi_n s} + 2kn\pi e^{-2kn\pi s} \right) \right) \left( \cos 2n\pi y - e^{-\frac{\alpha y}{k}} - e^{-\frac{\alpha(1-y)}{k}} \right) e^{it} \quad (32)$$

$$\tau_{xx}|_{s=0} = \mu\epsilon\omega \sum_{n=0}^{\infty} A_n \left( -2kn\pi + 4in^2\pi^2\delta^2 k^2 \left( -\xi_n + 2kn\pi \right) \right) \left( \cos 2n\pi y - e^{-\frac{\alpha y}{k}} - e^{-\frac{\alpha(1-y)}{k}} \right) e^{it} \quad (33)$$

Here  $\epsilon\omega$  is the dimensionalising factor for viscous stress tensor. Curvature is found from the interface deformation equation  $x - l(t, y) = 0$  as:

$$\kappa = i\epsilon e^{it} \sum_{n=0}^{\infty} A_n \left( -4n^2\pi^2 \cos 2n\pi y - \frac{\alpha^2}{k^2} \left( e^{-\frac{\alpha y}{k}} + e^{-\frac{\alpha(1-y)}{k}} \right) \right) \quad (34)$$

Substituting these expressions in the normal stress balance equation and collecting all the terms with  $y$  dependency, we get a set of equations from  $n=1$  to  $\infty$  as:

$$\begin{aligned} \left( -\frac{\omega^2}{2n\pi k} \left( 1 + \frac{8k^2 n^2 \pi^2}{\alpha^2} \right) + \frac{2\mu i \omega k n \pi}{\rho a^2} + \frac{4n^2 \pi^2 \gamma k}{\rho a^3} \right) A_n \\ - \frac{2i\mu\omega}{\rho a^2} \left( \frac{4\alpha (1 - e^{-\frac{\alpha}{k}})}{4n^2 \pi^2 + \alpha^2} \right) \sum_{m=1}^{\infty} A_m m \pi + \\ \frac{\alpha^2 \gamma}{\rho a^3 k^2} \left( \frac{4\alpha (1 - e^{-\frac{\alpha}{k}})}{4n^2 \pi^2 + \alpha^2} \right) \sum_{m=0}^{\infty} A_m = 0 \quad (35) \end{aligned}$$

We obtain another mathematical condition from the fact that the contact point must be stress free for it to be pinned. This indicates that the stream function obtained from boundary layer ( $\psi_{bl}$ ) must satisfy the tangential stress balance at the interface. On substituting  $\psi_{bl}$  in tangential stress balance equation 12 and simplifying, we obtain:

$$\sum_{n=0}^{\infty} A_n = O(\delta^2) \quad (36)$$

$A_n$ s are determined for a fixed set of  $N + 1$  modes, where  $N$  stands for maximum number of modes we compute for in this system. The value of  $A_n$ s decrease with increase in  $n$  thus the higher modes have a lower contribution to the dynamics of the system. This results in a set of coupled equations given by:

$$\begin{aligned} \left( -\frac{\omega^2}{2n\pi k} \left( 1 + \frac{8k^2 n^2 \pi^2}{\alpha^2} \right) + \frac{2\mu i \omega k n \pi}{\rho a^2} + \frac{4n^2 \pi^2 \gamma k}{\rho a^3} \right) A_n \\ - \frac{2i\mu\omega}{\rho a^2} \left( \frac{4\alpha (1 - e^{-\frac{\alpha}{k}})}{4n^2 \pi^2 + \alpha^2} \right) \sum_{m=1}^N A_m m \pi \\ + \frac{\alpha^2 \gamma}{\rho a^3 k^2} \left( \frac{4\alpha (1 - e^{-\frac{\alpha}{k}})}{4n^2 \pi^2 + \alpha^2} \right) \sum_{m=0}^N A_m = 0 \quad (37) \end{aligned}$$

$$\sum_{n=0}^N A_n = K \delta^2 \quad (38)$$

Equation 37 is a set of  $N$  equations such that  $n$  goes from 1 to  $N$ . We substitute Equation 38 in 37 and solve for this set of  $N$  equations using matrix inversion. The remainder  $A_0$  is obtained from Equation 38 as  $A_0 = K \delta^2 - \sum_{n=1}^N A_n$ .  $K$  is assumed to be a non-zero value ( $K = 0.1$ ). It is seen in our calculations that changing the value of  $K$  does not alter the results obtained. However, the value of  $K$  cannot be zero as it results in Equation 37 becoming trivial.

We express the interface deformation equation (Equation 28) in terms of a Fourier cosine series for ease of comparison with experiments and defining the steady streaming intensity. In the results discussed forward, the interface deformation is rewritten as  $\sum_{n=1}^N a_n \cos 2n\pi y$  and the  $a_n$ s are used for plotting and calculating streaming intensity. This will be discussed in the next section.

## V. RESULTS

### A. Mode amplitudes as a function of driving frequency

The Fourier mode amplitudes  $a_n$ s are plotted against the driving frequency to find the resonant frequency for each modes. In all calculations forward, we consider  $N = 20$  and  $M = 50$ . It is to be noted that the results are insensitive to the values of  $N$ ,  $M$  if they are above 5. Higher number of modes are used for better accuracy. Figure 3 shows the

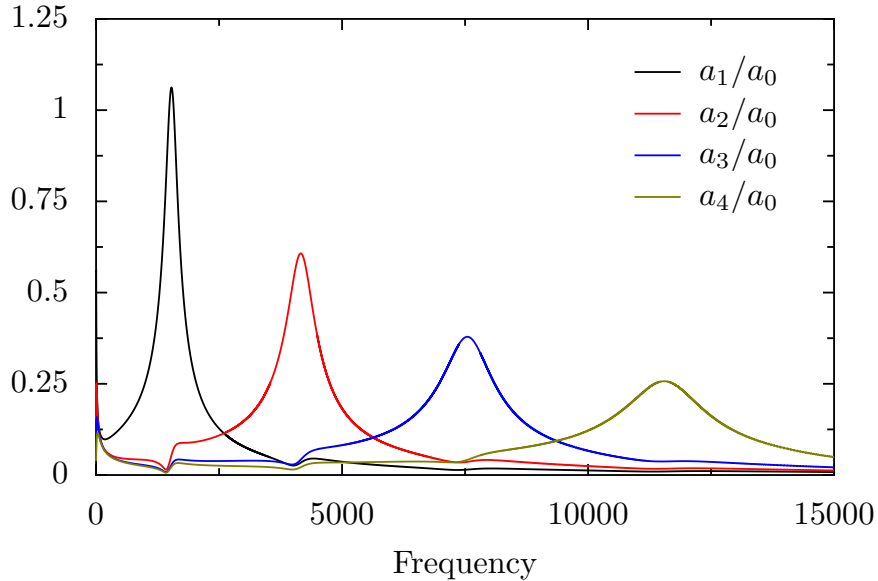


FIG. 3: The amplitude modes for a bubble of 1.6 mm length and 0.374 mm width with water as surrounding fluid, mimicking the experiments performed by Ryu *et.al.* [15] The maximum amplitude obtained is at 4.161 kHz for second order normalized modes (red) very close to 4 kHz found experimentally. Maxima for each amplitude modes occur at 1.533 kHz, 4.161 kHz, 7.547 kHz, and 11.545 kHz respectively.

different normalized mode amplitudes plotted against driving frequency for a bubble of 1.6

mm length and 0.374 mm width surrounded by water. The parameters are chosen as per the experiments of Ryu *et.al.* [15]. With increase in frequency, the different surface modes of oscillation become more prominent. The maximum amplitude of each succeeding mode is lower than the previous one. However, they become visible at higher frequencies, as their maxima is higher than the amplitude of other modes at that frequency. This is observed experimentally in both spherical<sup>14</sup> as well as semi – cylindrical<sup>4</sup> bubbles. The predicted resonance frequency, 4.161 kHz, is very close to the experimental value of 4 kHz obtained by Ryu *et.al.* [15] in his experiments. The experimental images of Ryu *et.al.* [15] show oscillations corresponding to a higher mode (not first mode) at the determined resonance frequency. This explains why the second peak obtained in our study coincides with the experimental resonance frequency obtained by Ryu *et.al.* [15]

### B. Leading order interface deformation

The  $A_n$  values are substituted in Equation 26 to determine the gas – liquid interface deformation. Figure 4 shows the periodic nature of interface deformation. It is observed that the leading order interface oscillations are periodic with time period of  $1/\omega$  as specified in the model.

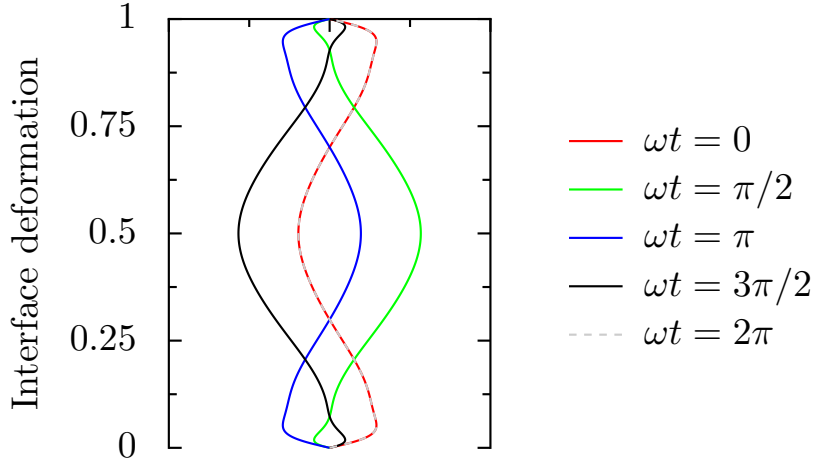


FIG. 4: Purely oscillatory interface deformation calculated for a bubble of 1.6 mm length and 0.374 mm width, surrounded by water and driven at 4 kHz.

We emphasize that the amplitude of interface deformation shown is to be scaled with  $\epsilon a$  which is a very small quantity. The magnified version is shown in Figure 4 to elaborate



that the velocity suddenly drops to zero in the wall boundary layer and hence the interface pinning is satisfied.

### C. Leading order velocity field

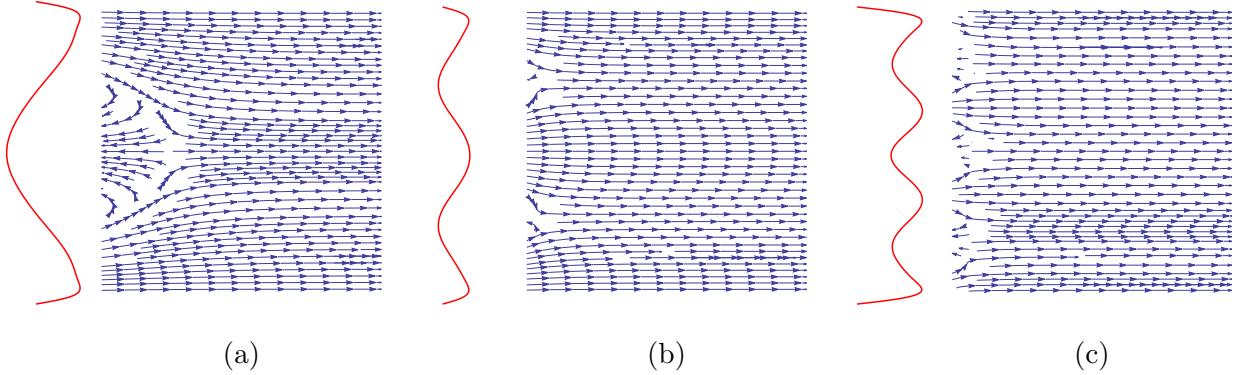


FIG. 5: Interface deformation and leading order velocity profile at frequencies: (a) 1.533 kHz (b) 4.161 kHz and (c) 7.547 kHz. Surrounding fluid is water and the frequencies chosen are the maxima of first second and third modes from Figure 3 respectively.

We plot the leading order velocity field by substituting the  $A_n$  values obtained from matrix inversion on equation 27. The  $e^{it}$  term in the expression suggests that the velocity field is harmonic in nature. In Figure 5, we see the interface deformation and its corresponding flow field generated by an inviscid slug of 1.6 mm length and 0.374 mm width, in water. At higher modes, higher number of vortices and interface modes are observed as predicted in Figure 3. Furthermore, the velocity field shown fluctuates with the frequency specified (i.e., the velocity vectors reverse direction periodically). These are inconceivable by the naked eye. The frequencies chosen are the peaks obtained in Figure 3 so as to show the contrast in modes seen on the interface.

The magnitude of Reynolds stress that drives the observable first order flow is also called as steady streaming intensity, can be predicted from leading order analysis. We use the concept of mixed mode streaming to predict the steady streaming intensity [17]. Mixed mode streaming considers the fact that the streaming velocity arises from an interaction of each mode with all other modes (For example,  $a_1$  can combine with  $a_0$ ,  $a_2$ ,  $a_3$  and so on) as the Reynolds stress is product of velocity and its gradient. The normalised steady streaming

intensity is defined as  $a_n/a_0 \sin(\phi_n - \phi_0)$  where  $a_n$ s are the Fourier surface mode amplitudes ( $n = 1, 2, 3, \dots$ ). This is because the combination of any mode with the volumetric mode  $a_0$  is always the strongest. Here  $a_0$  is used to normalise the amplitudes and streaming intensity so as to obtain a relative amplitude.

#### D. Comparison with experimental data

We also simulate the experiments of Ryu *et.al.* [15] by varying the aspect ratio or  $k$  values. Ryu *et.al.* brings a cylindrical tube very close to a sessile microbubble such that the rim of the tube coincides with the bubble interface and finds the maximum velocity observed in the tube. A comparison of the setup by Ryu *et.al.* [15] and the theoretical model by us is shown in Figure 6. For comparison, we extract the exact distance of the tube from the bottom of the bubble trigonometrically ( $\sqrt{R^2 - r^2}/2$ ) and use as  $a$  in our calculations. Further,  $b$  is taken as the diameter of the tube ( $2r$ ).

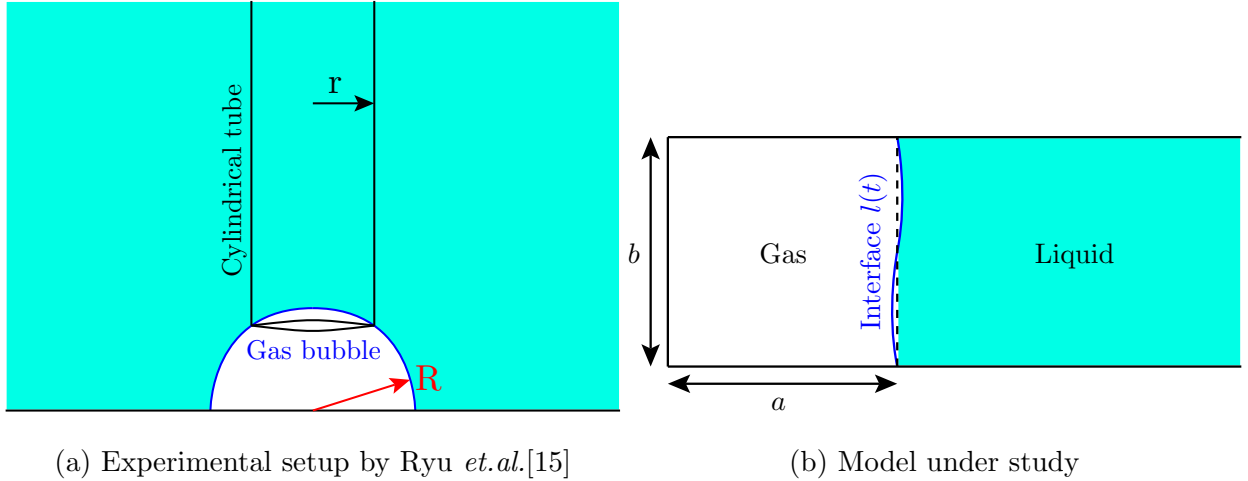


FIG. 6: Side - by - side comparison of the model and experimental setup

The streaming intensity obtained in our study ( $a_2/a_0 \sin \phi_2 - \phi_0$ ) (See Figure 7) follows the trend given by Ryu *et. al.* The streaming intensity is the magnitude of Reynolds stress that drives the higher order observable flow. However, the streaming intensity obtained is proportional to the streaming velocity for lower tube diameters. This is expected because the interface coinciding with the tube becomes flat as the radius of the tube decreases. The streaming intensity obtained from our study is considerably lower than the velocity obtained

by Ryu.*et.al.* [15] We attribute this to the fact that the intensity term is to be multiplied by Reynolds number before determining the first order velocity. As the tube to bubble diameter ratio increases, the interface becomes more and more curved and so it deviates from the current model which considers a flat interface at base state. This explains the deviant increase in streaming intensity predicted by our model at higher aspect ratios.

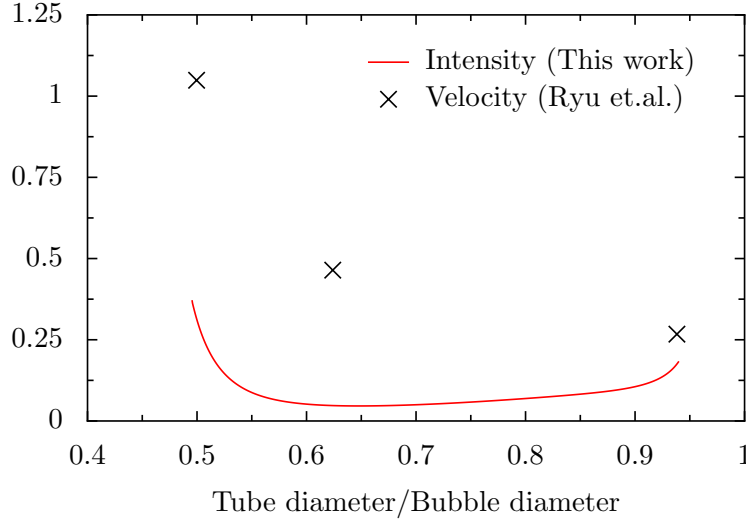


FIG. 7: Our study follows the same trend as Ryu et. al.'s experimental results. They do not match exactly because the steady intensity is dimensionless in nature and is a measure of the magnitude of Reynolds stress that drives the higher order observable flow

Next, we study the effect of aspect ratio on resonance frequency of each mode in the system. We see that the resonance frequency for each mode decreases with increase in length of slug/bubble for a given continuous phase (See Figure 8). This also means that the energy and operating cost required to drive the flow is lesser for larger bubbles.

We qualitatively compare the resonant frequency dependence on aspect ratio found from this study with the dependency of Minnaert frequency of a prolate spheroid bubble on the ratio of major to minor axis. For a prolate spheroid the Minnaert frequency is given by:

$$f_{Minnaert} = \frac{1}{2\pi} \sqrt{\frac{\gamma P_0 C}{\rho V_0}} \quad (39)$$

Where,  $C = 8\pi a \sqrt{1 - k^{-2}} \left( \ln \left( \frac{1 + \sqrt{1 - k^{-2}}}{1 - \sqrt{1 - k^{-2}}} \right) \right)^{-1}$ ,  $k = \frac{\alpha}{\beta}$  where  $\alpha$ ,  $\beta$  represent the major and minor axis of the spheroid [24]. From Equation 39, directly correlating  $\alpha$ ,  $\beta$  to the length  $a$  and width  $b$  of the bubble in this work (See Figure 1), and  $P_0$ ,  $V_0$  to  $p_{ch}$  and volume of

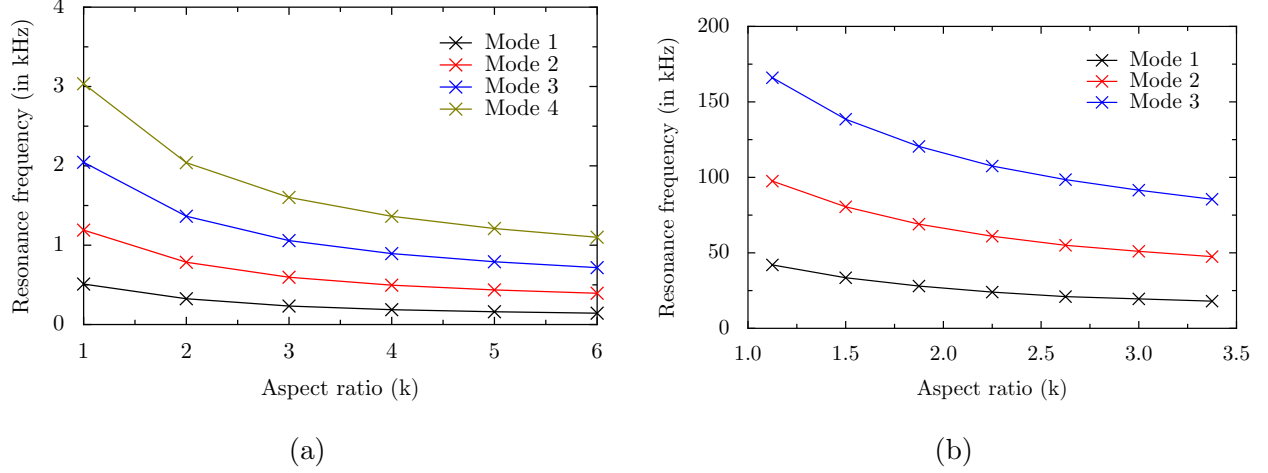


FIG. 8: Resonance frequency variation with increase in aspect ratio for milli (a) and micro (b) channels. Fluid properties correspond to water at room temperature. The width of the channel  $b$  values are (a) 1.6 mm and (b) 80  $\mu$ m.

the cuboidal bubble, we obtain the corresponding Minnaert frequency in this work to be proportional to  $F$  such that:

$$F = \sqrt{\frac{1}{b} \sqrt{1 - k^{-2}} \left( \ln \left( \frac{1 + \sqrt{1 - k^{-2}}}{1 - \sqrt{1 - k^{-2}}} \right) \right)^{-1}} \quad (40)$$

In Figure 9, the trend shown by Minnaert frequency is a continuous decrease as predicted

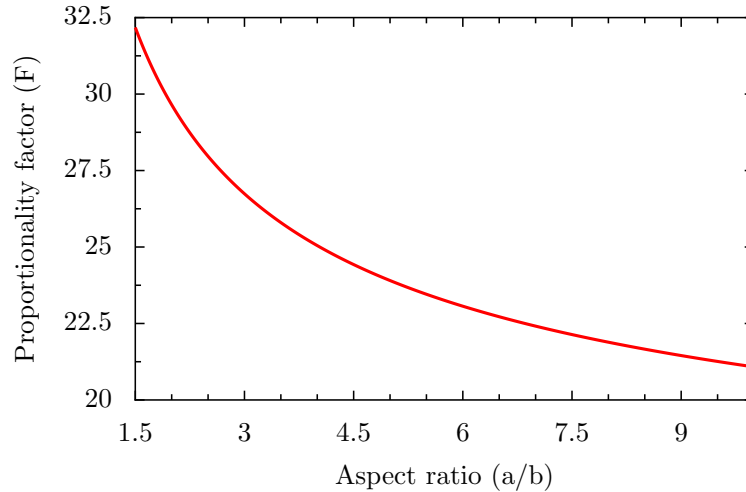


FIG. 9:  $F$  v/s aspect ratio ( $k$ ) for a prolate spheroid with minor axis fixed at 0.374 mm and major axis varied. Surrounding fluid is water at room temperature.  $F$  is proportional to Minnaert frequency which is analogous to the resonant frequency in our system.

by the present model. We further emphasize that Minnaert frequency is calculated for an isolated bubble as opposed to the lodged bubble system studied in this work. A similar decreasing resonance frequency trend is also observed by Jang *et.al.* [25] for a spherical bubble trapped in a cylindrical tube.

## VI. CONCLUSIONS

This work focusses on developing a theoretical framework to modelling the flow field generated by channel geometry specific to that of an acoustic micropump/micromixer from a simple leading order analysis. We show that a cartesian system is enough to predict the resonant frequency of a trapped gas slug system operating at high Strouhal numbers. By introducing differential scaling along  $x$  and  $y$  coordinates, we have brought forth the length of side- channel, used for trapping the oscillating bubble in experiments, into the calculations. This length of side-channel has been ignored in almost all analytical studies because of semi - cylindrical or spherical shape of bubble. However, our study shows that resonance frequency and streaming intensity are functions of the length of side-channel. The streaming intensity calculated from leading order analysis qualitatively matches the experiments of Ryu *et.al.* [15]. We also predict that resonance frequency associated with the trapped bubble commonly used for micropumping and micromixing will decrease with increase in length of bubble, implying that the energy requirement to drive longer bubbles will be lower. The decreasing trend of resonance frequency obtained from this study is also observed for Minnaert frequency of a prolate spheroid. The length and width of slug is assumed analogous to major and minor axis of the spheroid.

- 
- [1] N. Riley, Steady streaming, Annual Review of Fluid Mechanics **33**, 43 (2001).
  - [2] S. J. Lighthill, Acoustic streaming, Journal of Sound and Vibration **61**, 391 (1978).
  - [3] X. Ding, S. C. S. Lin, B. Kiraly, H. Yue, S. Li, I. K. Chiang, J. Shi, S. J. Benkovic, and T. J. Huang, On-chip manipulation of single microparticles, cells, and organisms using surface acoustic waves, Proceedings of the National Academy of Sciences of the United States of America **109**, 11105 (2012).

- [4] C. Wang, B. Rallabandi, and S. Hilgenfeldt, Frequency dependence and frequency control of microbubble streaming flows, *Physics of Fluids* **25**, 022002 (2013), <https://doi.org/10.1063/1.4790803>.
- [5] D. Ahmed, X. Mao, J. Shi, B. K. Juluri, and T. J. Huang, A millisecond micromixer via single-bubble-based acoustic streaming, *Lab Chip* **9**, 2738 (2009).
- [6] A. Hashmi, G. Yu, M. Reilly-Collette, G. Heiman, and J. Xu, Oscillating bubbles: a versatile tool for lab on a chip applications, *Lab Chip* **12**, 4216 (2012).
- [7] J. Li, A. Crivoi, X. Peng, L. Shen, Y. Pu, Z. Fan, and S. Cummer, Three dimensional acoustic tweezers with acoustic vortex streaming, (2021).
- [8] B. Davidson and N. Riley, Cavitation microstreaming, *Journal of Sound and Vibration* **15**, 217 (1971).
- [9] R. Thameem, B. Rallabandi, and S. Hilgenfeldt, Particle migration and sorting in microbubble streaming flows, *Biomicrofluidics* **10**, 014124 (2016).
- [10] Y. Li, X. Liu, Q. Huang, and T. Arai, Controlled rotation of micro-objects using acoustically driven microbubbles, *Applied Physics Letters* **118**, 063701 (2021), <https://doi.org/10.1063/5.0038789>.
- [11] C. C. Coussios and R. A. Roy, Applications of acoustics and cavitation to noninvasive therapy and drug delivery, *Annual Review of Fluid Mechanics* **40**, 395 (2008), <https://doi.org/10.1146/annurev.fluid.40.111406.102116>.
- [12] M. S. Longuet-Higgins, Viscous streaming from an oscillating spherical bubble, *Proceedings: Mathematical, Physical and Engineering Sciences* **454**, 725 (1998).
- [13] S. A. Elder, Cavitation microstreaming, *The Journal of the Acoustical Society of America* **31**, 54 (1959).
- [14] P. THO, R. MANASSEH, and A. OOI, Cavitation microstreaming patterns in single and multiple bubble systems, *Journal of Fluid Mechanics* **576**, 191–233 (2007).
- [15] K. Ryu, S. K. Chung, and S. K. Cho, Micropumping by an acoustically excited oscillating bubble for automated implantable microfluidic devices, *Journal of the Association for Laboratory Automation* **15**, 163 (2010), <https://doi.org/10.1016/j.jala.2010.01.012>.
- [16] T. Peng, M. Zhou, S. Yuan, and B. Jiang, Trapping stable bubbles in hydrophobic microchannel for continuous ultrasonic microparticle manipulation, *Sensors and Actuators A: Physical* **331**, 113045 (2021).

- [17] B. Rallabandi, C. Wang, and S. Hilgenfeldt, Two-dimensional streaming flows driven by sessile semicylindrical microbubbles, *Journal of Fluid Mechanics* **739**, 57–71 (2014).
- [18] A. Etminan, Y. S. Muzychka, and K. Pope, A review on the hydrodynamics of taylor flow in microchannels: Experimental and computational studies, *Processes* **9**, 10.3390/pr9050870 (2021).
- [19] S. Orbay, A. Ozcelik, J. Lata, M. Kaynak, M. Wu, and T. J. Huang, Mixing high-viscosity fluids via acoustically driven bubbles, *Journal of micromechanics and microengineering : structures, devices, and systems* **27** (2017).
- [20] S. Mohanty, J. Zhang, J. M. McNeill, T. Kuenen, F. P. Linde, J. Rouwkema, and S. Misra, Acoustically-actuated bubble-powered rotational micro-propellers, *Sensors and Actuators B: Chemical* **347**, 130589 (2021).
- [21] L. Yang, F. Xu, Q. Zhang, Z. Liu, and G. Chen, Gas-liquid hydrodynamics and mass transfer in microreactors under ultrasonic oscillation, *Chemical Engineering Journal* **397**, 125411 (2020).
- [22] M. Fauconnier, J.-C. Béra, and C. Inserra, Nonspherical modes nondegeneracy of a tethered bubble, *Phys. Rev. E* **102**, 033108 (2020).
- [23] F.-W. Liu, Y. Zhan, and S. K. Cho, Propulsion reversal in oscillating-bubble powered micro swimmer, *Journal of Micromechanics and Microengineering* **31**, 084001 (2021).
- [24] K. S. Spratt, K. M. Lee, P. S. Wilson, and M. S. Wochner, On the resonance frequency of an ideal arbitrarily-shaped bubble, *Proceedings of Meetings on Acoustics* **20**, 045004 (2013), <https://asa.scitation.org/doi/pdf/10.1121/1.4874614>.
- [25] N. W. Jang, S. M. Gracewski, B. Abrahamsen, T. Buttaccio, R. Halm, and D. Dalecki, Natural frequency of a gas bubble in a tube: experimental and simulation results, *The Journal of the Acoustical Society of America* **126**, EL34—40 (2009).